Supporting Information

Synthesis, structures, and reactivity of isomers of [RuCp*(1,4-(Me$_2$N)$_2$C$_6$H$_4$)]$_2$

Elena Longhi,[a] Chad Risko,[b] John Bacsa,[c] Victor Khrustalev,[d,e] Sergei Rigin,[d] Karttikay Moudgil,[a] Tatiana V. Timofeeva,[d] Seth R. Marder[a,f,g,h,i] and Stephen Barlow*[a,f]

[a.] School of Chemistry and Biochemistry & Center for Organic Photonics and Electronics, Georgia Institute of Technology, Atlanta, GA 30332-0400, USA.

[b.] Department of Chemistry & Center for Applied Energy Research (CAER), University of Kentucky, 125 Chemistry-Physics Building, Lexington, KY 40506, USA.

[c.] Crystallography Lab, Emory University, 201 Dowman Drive, Atlanta, GA 30322, USA.

[d.] Department of Chemistry, New Mexico Highlands University, Las Vegas, NM 87701, USA.

[e.] Department of Inorganic Chemistry, Peoples' Friendship University of Russia, Moscow 117198, Russia.

[f.] Renewable and Sustainable Energy Institute (RASEI), University of Colorado Boulder, Boulder, CO 80303, USA. E-mail: stephen.barlow@colorado.edu

[g.] Department of Chemical and Biological Engineering , University of Colorado Boulder, Boulder, CO 80303, USA.

[h.] Department of Chemistry, University of Colorado Boulder, Boulder, CO 80303, USA.

[i.] Chemistry and Nanoscience Center, National Renewable Energy Laboratory, Golden, CO 80401, USA.

S1. Additional details of structures of [RuCp*(arene)]⁺ salts

Table S1. Selected crystallographically determined structural parameters (Å, °) for $[RuCp^*(C_6R_nX_mH_{6-n-m})]^+$ (R = alkyl; X = NMe_2, O^-)

Cpd	r(Ru–CH/CR) [a]	r(Ru—CX) [b]	r(C—X) [c]	α [d]	β [e]	Σ(C-N-C) [f]	γ [g]
2⁺PF₆⁻ [h]	2.177(4)-2.194(3)	–	–	1.1	–	–	–
3⁺PF₆⁻	2.215(3)-2.230(3)	2.323(3)	1.369(4)	1.9	7.3	358.7(9)	5.2
4⁺PF₆⁻	2.204(4)-2.214(4)	2.340(4), 2.310(4)	1.359(5), 1.374(5)	2.0	8.6, 7.5	358.5, 354.3	9.1, 10.3
I⁺BF₄⁻ [ij]	2.19(1)-2.230(9)	2.347(9)	1.37(1)	3.1	8.1	354.1	7.2
II•2PhOH [ik]	2.186(6)-2.211(6)	2.34	1.284(7)	3.1	7.4	–	–
III [il]	2.183(3)-2.300(3)	2.56	1.256(4)	7.2	19.0	–	–

[a] Bond lengths between the Ru and the η^6-arene C atoms without π-donor (X) substitution. [b] Bond lengths between the Ru and the η^6-arene C atom(s) with X substitution. [c] Bond length between the X-substituted arene C atom(s) and the attached X atom(s). [d] Ring tilt between the planes formed by the coordinated Cp* C atoms and the plane by the 5 (or 6 in the case of **2⁺** or 4 in the case of **4⁺**) arene C atoms without π-donor (X) substitution. [e] Fold angle(s) between the plane formed by each X-substituted carbon and its two adjacent carbon atoms and the plane formed by the 5 (or 4 in the case of **4⁺**) arene C atoms without X substitution. [f] Sum of C—N—C bond angles in the NMe_2 group(s). [g] Torsion angle(s) around the Arene—NMe_2 bond(s), each defined as the angle between the plane formed by the NMe_2-substituted C and the 3 atoms to which it is bound, and the plane formed by the N atom and the 3 atoms to which it is bound. See also Fig. S1. [h] Ref. 1. [i] See Scheme 3 for molecular structures. [j] Ref. 2. [k] Ref. 3. [l] Ref. 4.
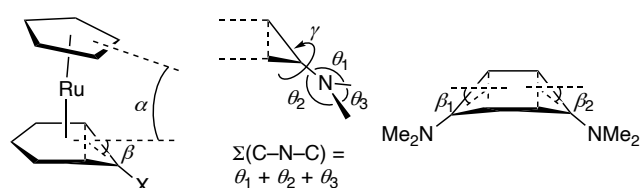

Fig. S1. Schematic representation of some of the structural parameters for π-donor-substituted [RuCp*(arene)]⁺ structures compared in Table S1 and discussed below. See footnote to Table S1 for more detailed definitions.

As discussed in the main text, one feature exhibited by **3⁺** and **4⁺**, but not **2⁺**, is that the arene ligands are slightly folded, as quantified by the angle β (Table S1, Fig. S1), such that the Ru—CN bonds are somewhat longer than the bonds to the other arene carbon atoms, or than Ru–C_{arene} bonds in typical [RuCp*(arene)]⁺ cations. As indicated in Table S1, similar folds have previously been reported, however, for the structures of other cations with π-donor arene substituents, notably [RuCp*($C_6H_5NMe_2$)]⁺BF₄⁻ (**I⁺**BF₄⁻)[2] and RuCp*(C_6H_5O)•2PhOH (**II•2PhOH**)[3] (Ru-CO 2.34 Å); these can be regarded as a distortion towards a structure in which the arene becomes an η^5-cyclohexadienyl ligand with an exo-iminium or carbonyl group (Scheme 3). In the cases of **3⁺**, **4⁺**, and **I⁺**, the amine groups are close to planar (Σ(C-N-C) is close to 360°) and close to coplanar with the plane formed by the amino-substituted atom and the two atoms on the fold line (as defined by small values of γ, see Table S1 and Fig. S1), also consistent contributions of η^5-cyclohexadienyl structures.
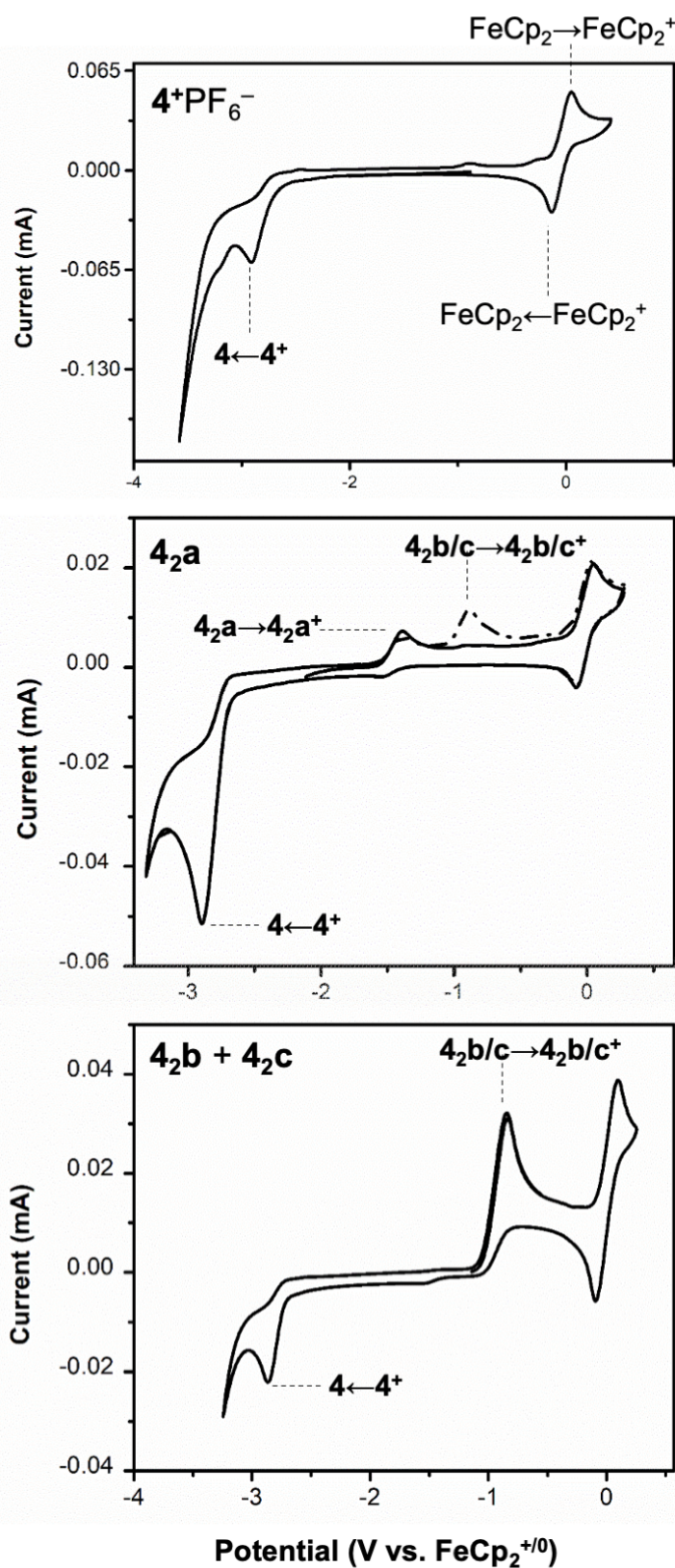
S2. Electrochemical data

Fig. S2. Cyclic voltammograms of **4⁺**, **4₂a**, and **4₂b+4₂c** in THF / 0.1 M of NBu₄PF₆ as electrolyte at a scan rate of 0.1 Vs⁻¹ (with ferrocene as an internal standard). In **4₂a** the dashed line shows the second cycle: after scanning beyond the monomer reduction potential, the oxidation peak at ca. –0.88 V vs FeCp₂⁺/⁰ appears, suggesting the formation of **4₂b** and/or **4₂c**.
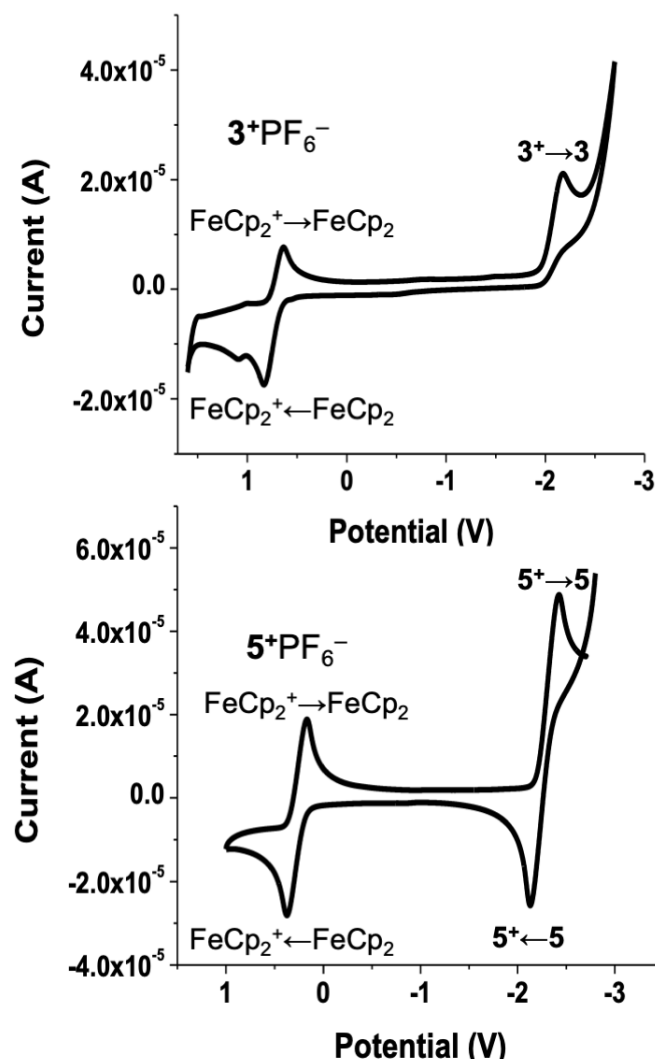
Fig. S3. Cyclic voltammograms of **3⁺** and **5⁺** in THF / 0.1 M of NBu₄PF₆ as electrolyte at a scan rate of 0.05 Vs⁻¹ (with ferrocene as an internal standard). Note that the oxidation wave see subsequent to reduction of **3⁺** is more anodic than that of ferrocene, suggesting that the product of reduction is not a dimer, and that the reduction of **5⁺** appears reversible at this scan rate (clearly **5** is unstable on a longer timescale as diamagnetic species are obtained following chemical reduction).

S3. Characterization of 5⁺PF₆⁻ and its deprotonation product, 6

[RuCp*(1,3,5-^{t}Bu₃C₆H₃)]⁺PF₆⁻ (5⁺PF₆⁻). Obtained using the general procedure as a white solid (1.86 g, 49%) from [RuCp*(NCMe)₃]⁺PF₆⁻ (3.00 g, 6.0 mmol) and 1,3,5-tri-*tert*-butylbenzene (11.9 g, 48.6 mmol). ¹H NMR (300 MHz, acetone-d_6): δ 6.12 (s, 3H, arene C*H*), 1.43 (s, 15H, Cp* C*H₃*), 0.00 (s, 27H, ^{t}Bu C*H₃*). ¹³C{¹H} NMR (125 MHz, acetone-d_6): 117.84, 96.07, 79.92, 35.80, 31.03, 12.38. Anal. Calcd. for C₂₈H₄₅F₆PNRu: C, 53.58; H, 7,23. Found: C, 53.37; H, 7.16. MS (ESI) *m/z* 483.2 ([M–PF₆]⁺).

Reduction of 5⁺PF₆⁻. This reaction was carried out using Na:Hg and Na:K following procedures analogous to those previously described for dimerizations of **1⁺**PF₆⁻ and **2⁺**PF₆⁻, but product mixtures were obtained. When sodium naphthalenide was used as the reducing agent in THF, one of these products dominated (but was not fully purified) and could be identified as Ru(η^4-C₄Me₄C=CH₂)(η^6-1,3,5-^{t}Bu₃C₆H₃), **6**, using ¹H and ¹³C{¹H}, DEPT, HSQC, HMBC, and NOE NMR spectra. ¹H NMR (300 MHz, benzene-d_6): δ 5.36 (s, 3H, arene C*H*), 3.02 (s, 2H, C*H₂*), 1.83 (s, 6H, C₄Me₄C=CH₂ 2,3-Me C*H₃*), 1.73 (s, 6H, C₄Me₄C=CH₂ 1,4-Me C*H₃*), 1.22 (s, 27H, ^{t}Bu C*H₃*). ¹³C{¹H} NMR (125 MHz, benzene-d_6): 151.74 (*C*=CH₂ q), 105.11 (arene *C*^{t}Bu q), 88.60 (C₄Me₄C=CH₂ 2,4-*C*Me q), 76.18 (arene *C*H), 66.78 (C₄Me₄C=CH₂ 2,3-*C*Me q), 60.9 (*C*H₂), 34.71 (^{t}Bu C*H₃*), 34.02 (^{t}Bu *C*(CH₃)₃ q), 13.46 (C₄Me₄C=CH₂ 2,3-Me C*H₃*), 13.13 (C₄Me₄C=CH₂ 1,4-Me C*H₃*).
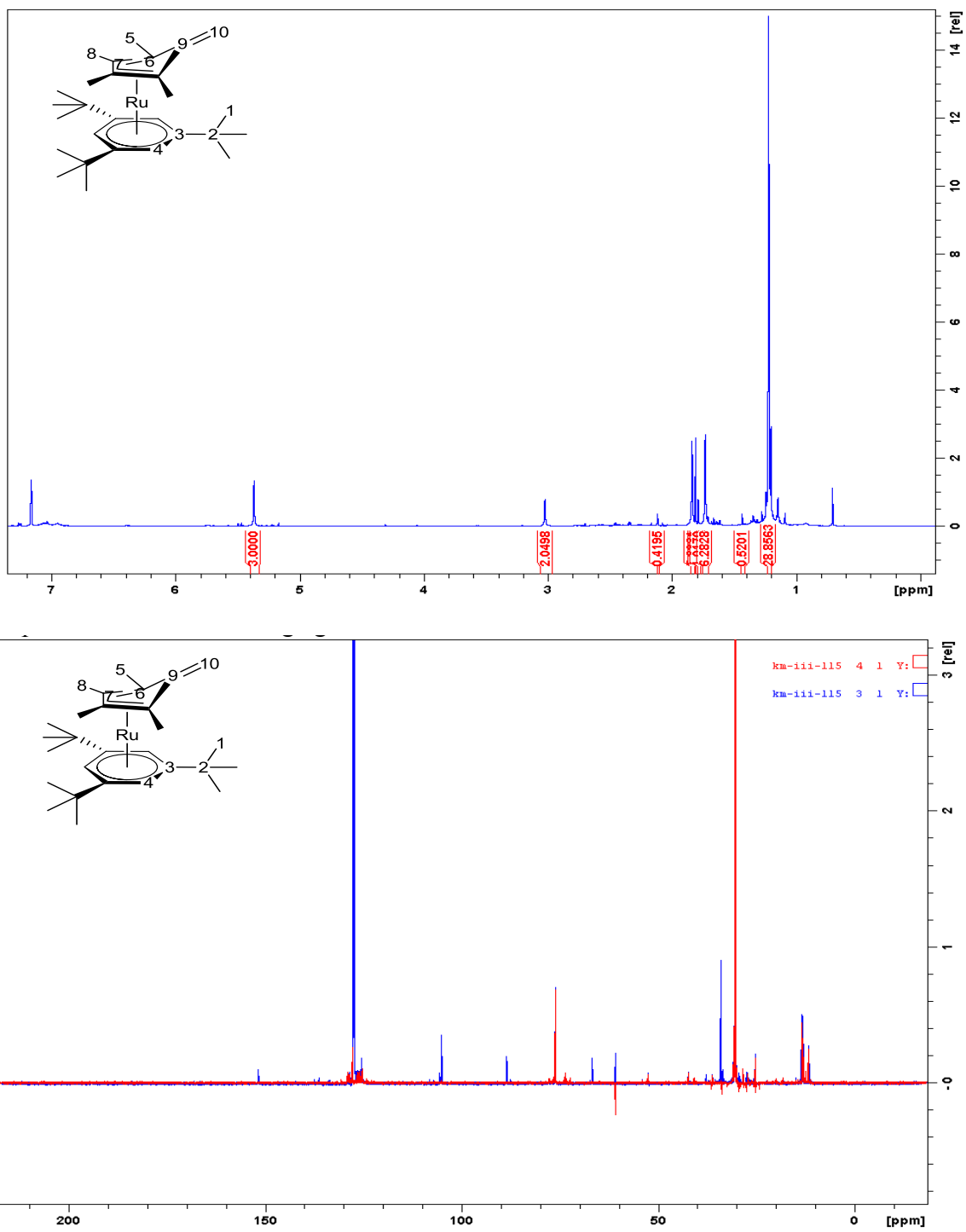
4

Fig. S4. ¹H (top), ¹³C{¹H} (bottom, blue), and DEPT-135 (bottom, black) spectra in C_6D_6 of the product obtained through reaction of **5**⁺PF₆⁻ with sodium naphthalenide in THF.
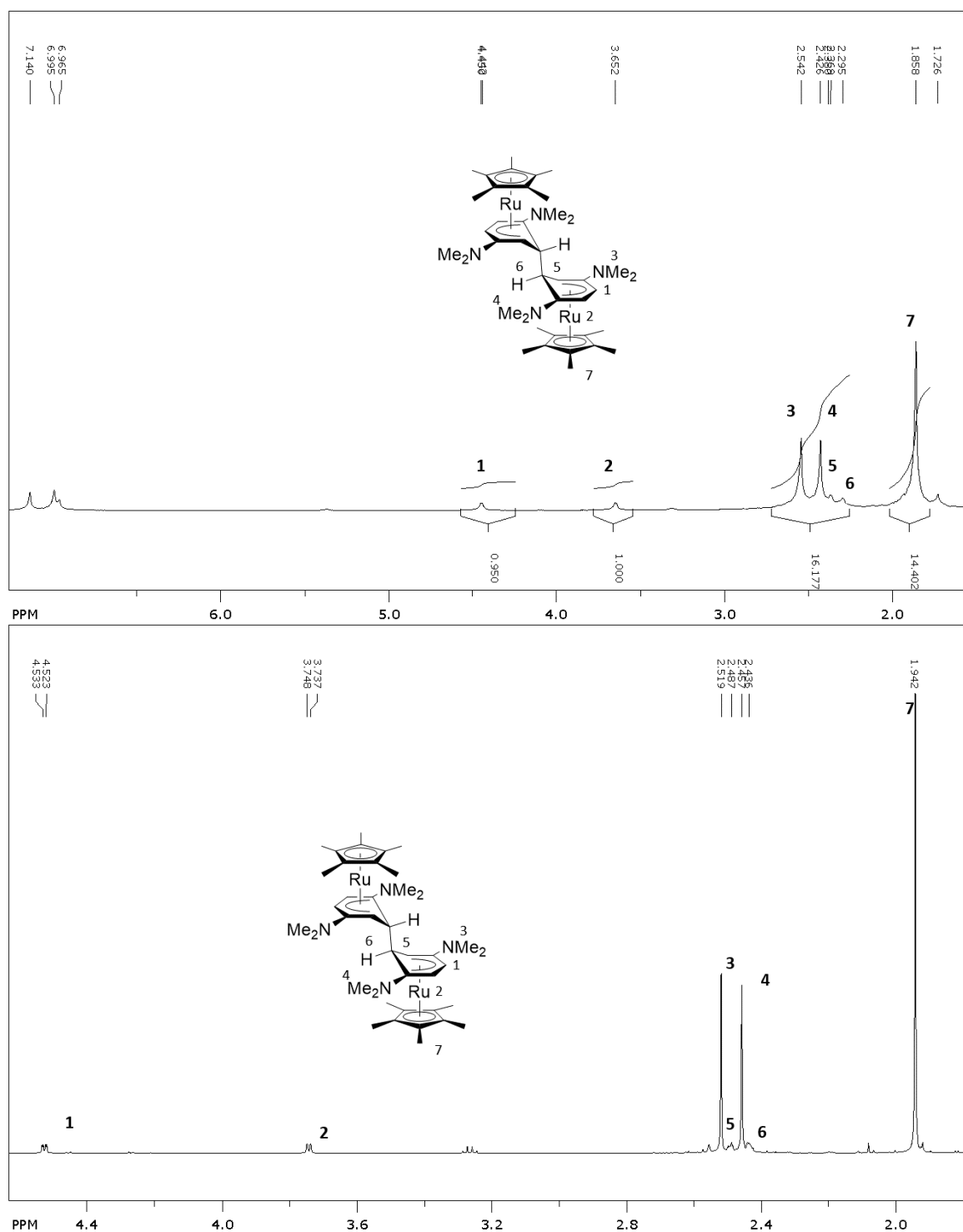
5

S4. NMR spectra of 4_2 isomers

Fig. S5. ^{1}H NMR spectra of **4_2a** in C_6D_6 with assignments. The 5 and 6-resonances are more clearly shown in the top spectrum, while [1]H-^{1}H coupling is better resolved in the lower spectrum.
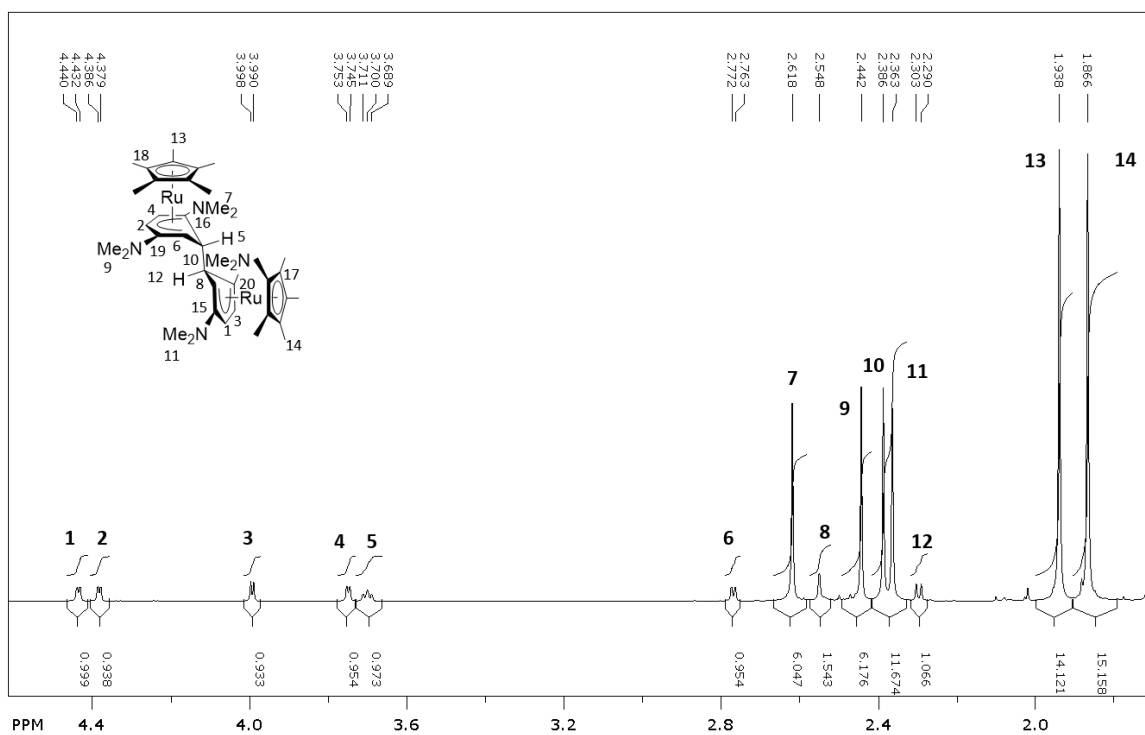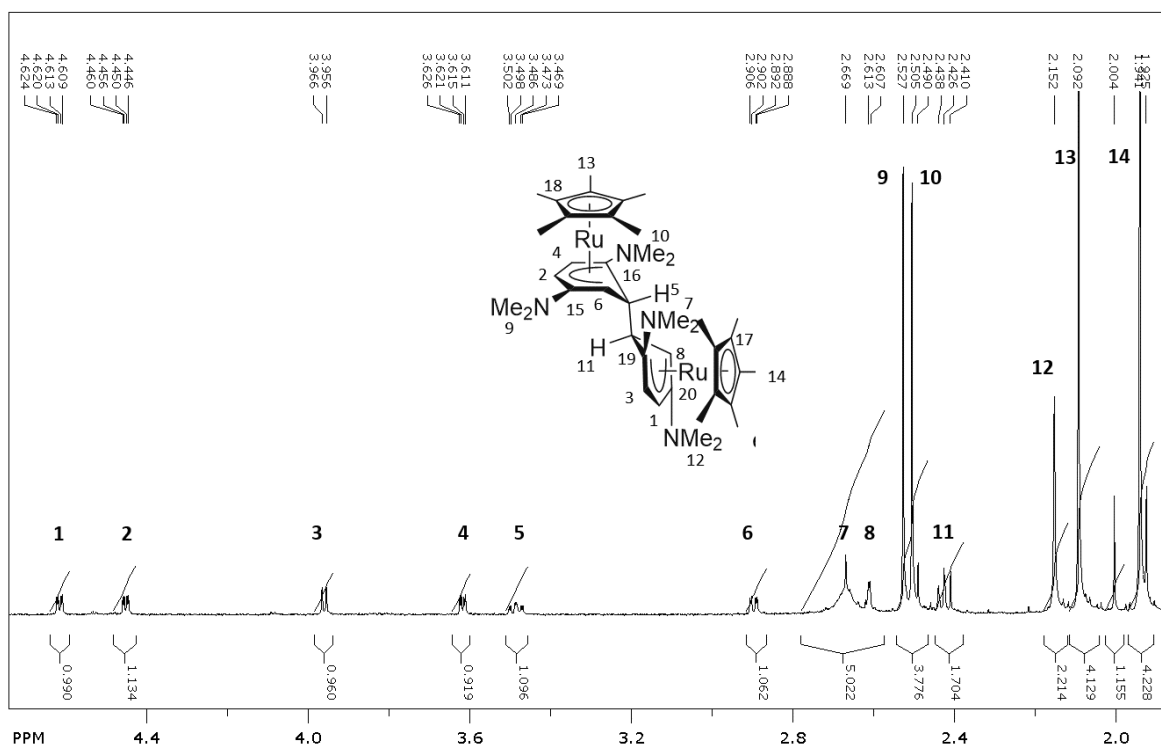
Fig. S6. ^{1}H NMR spectrum of **4$_2$b** in C$_6$D$_6$ with assignments.

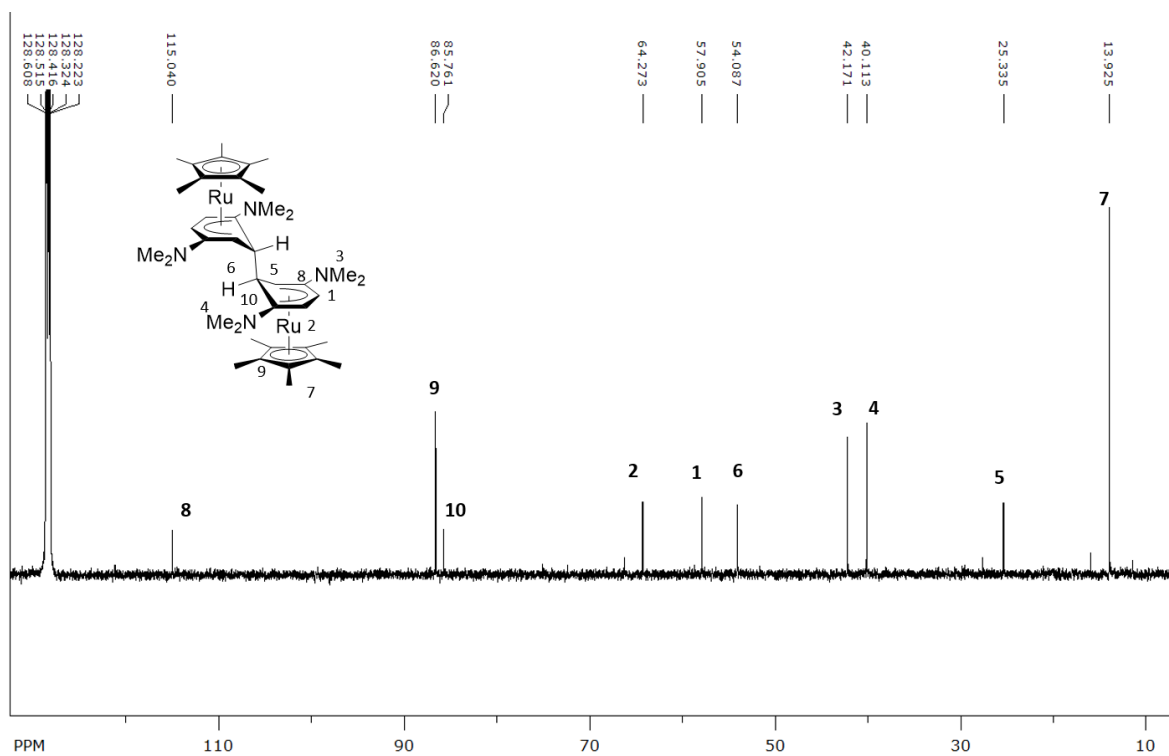**Fig. S7.** ^{1}H NMR spectrum of **4$_2$c** in C$_6$D$_6$ with assignments.

7

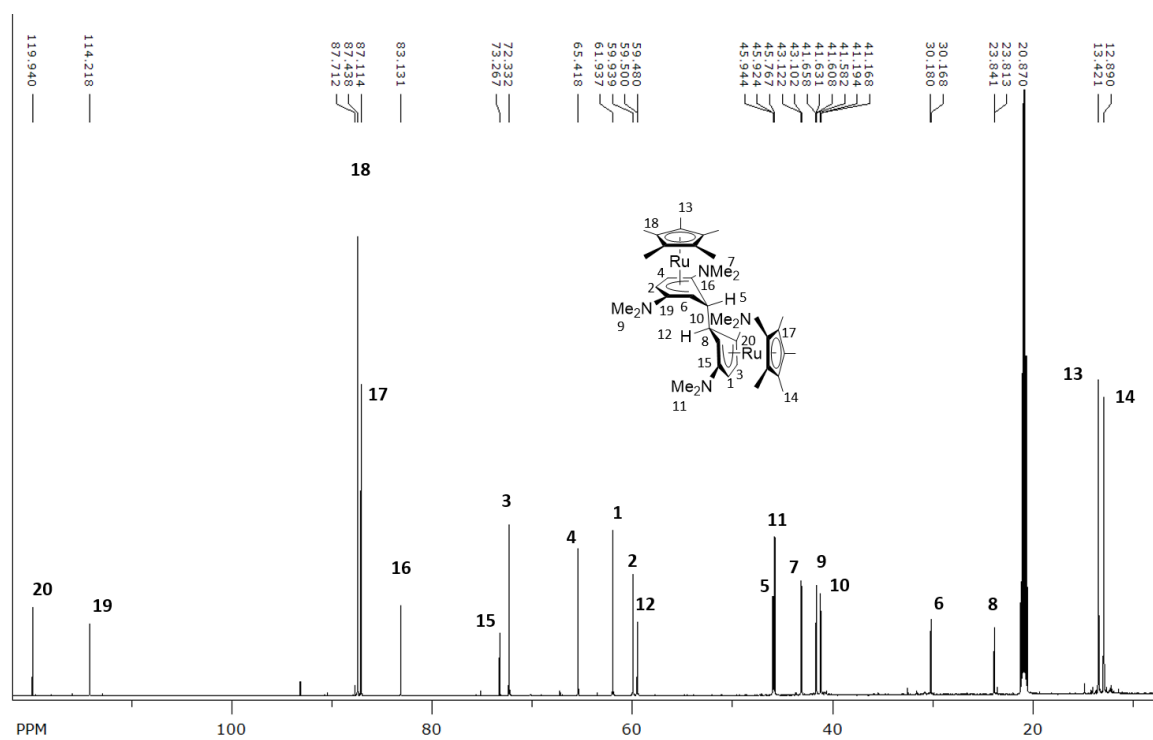**Fig. S8.** $^{13}C\{^1H\}$ NMR spectrum of **4$_2$a** in C_6D_6 with assignments.

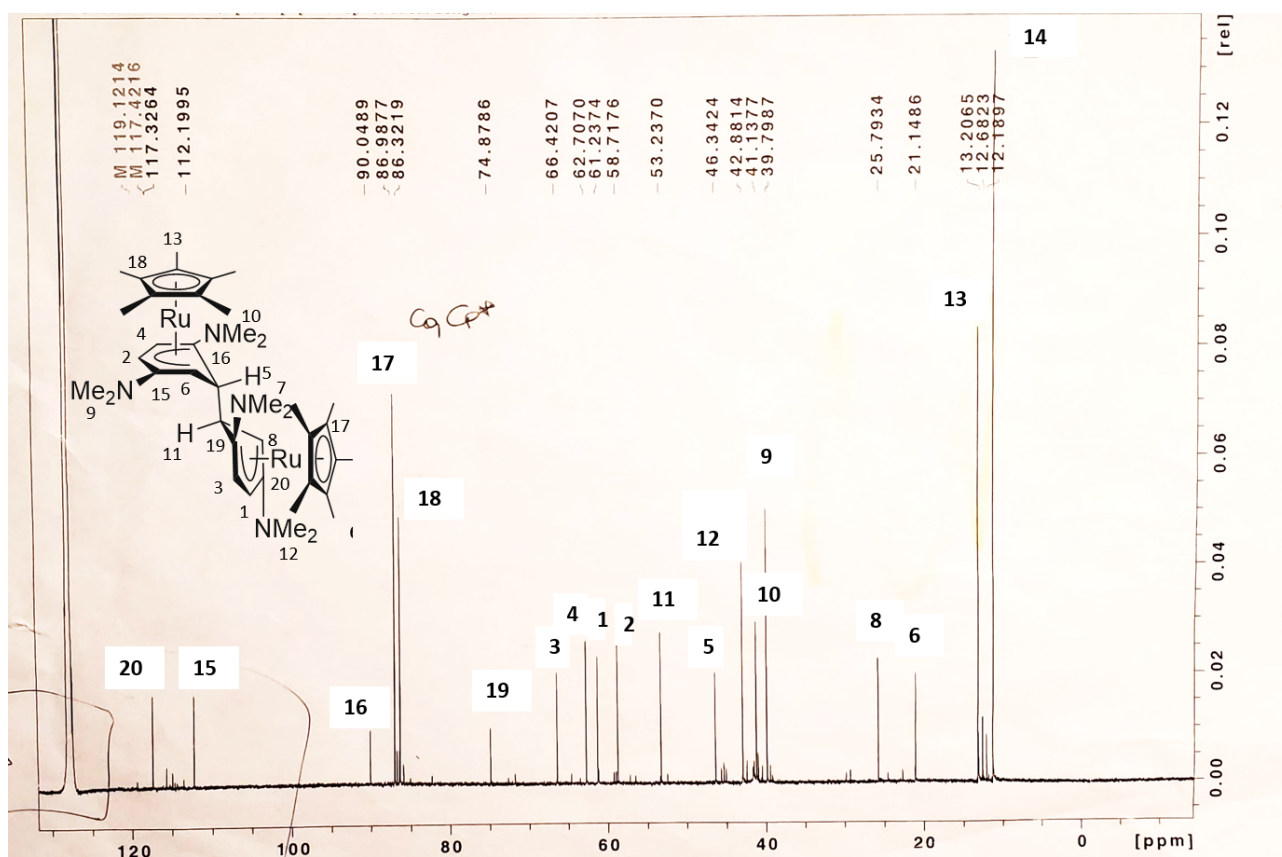**Fig. S9.** $^{13}C\{^1H\}$ NMR spectrum of **4$_2$b** in $C_6D_5CD_3$ with assignments.

Fig. S10. $^{13}C\{^1H\}$ NMR spectra of **4₂c** in C_6D_6 with assignments.

Discussion of NMR coupling constant and chemical shifts for *exo,endo* isomers of 4₂. The observed 3-bond ^1H-^1H coupling constants, ^3J, for the *ipso* (bridgehead) and *ortho* (adjacent to bridgehead) CH resonances for **4₂b** are consistent with the crystallographically determined structure; specifically, the CH*ipso*-CH*ortho* coupling constant in the *endo*-linked ring is much smaller than the other three-bond CH—CH couplings, consistent with a H–C–C–H torsion angle in the crystal structure close to the 90° at which the Karplus equation predicts ^3J to be minimized (Fig. S11). Interestingly, the bridgehead CH resonance of the *exo*-connected monomer of **4₂b** is also seen at considerably lower field (3.7 ppm) than that of the bridgehead CH resonances of **1₂**,[5] **2₂**,[6] or **4₂a** (all *exo,exo*-connected, 1.8-2.5 ppm) or the CH*ipso* of the *endo*-connected monomer of **4₂b** (2.3 ppm). This can also be correlated to the crystal structures, which show the bridgehead CHs of the *exo,exo* structures are positioned close to the center of the pentadienyl π-system of the other monomer, and thus experience shielding by the π-system (the distances from H*ipso* to the centroid of Ru coordinated carbons in **2₂** and **4₂a** are 2.47 and 2.51 Å, respectively). A fairly close approach to the centroid of the pentadienyl unit of the other monomer is also seen for the *endo*-connected monomer H*ipso* of **4₂b** (2.60 Å, Fig. S11), whereas the *exo*-connected monomer H*ipso* does not closely approach the neighboring π-system and, therefore, is more deshielded.
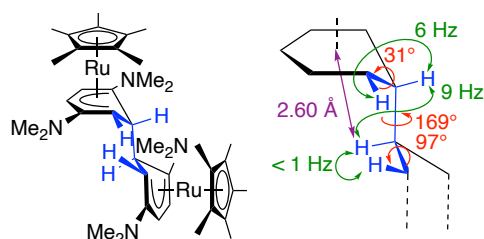

Fig. S11. Three-bond ^1H-^1H coupling constants (green) and crystallographically determined H–C–C–H torsion angles (red) and CH*ipso,endo*...centroid*exo* approach (purple) for **4₂b**.

9

4₂c exhibits qualitatively similar NMR spectra to **4₂b**, supporting the similar proposed structure. In particular the ring CH resonances exhibit similar patterns of coupling constants and chemical shifts. DFT calculations indicate that a molecule with the structure proposed for **4₂c** would exhibit similar CH_{ipso}—CH_{ortho} torsions (40 and 90° for *exo*- and *endo*-connected monomers) and *endo*-monomer H_{ipso} to *exo*-monomer π-system approach (2.86 Å) to those seen for the crystal and calculated structures of **4₂b**. One of the NMe₂ resonances for **4₂c**, assigned to the *ortho* NMe₂ group of the *endo*-connected monomer, is also rather broad. In the DFT-calculated structure of **4₂c** this NMe₂ group closely approaches the π-system of the *exo*-connected monomer; one of the methyl carbon atoms is 3.19 Å from the NMe₂-substituted *meta*-C and the nitrogen atom is 2.96 Å from the unsubstituted *ortho*-C. This close approach presumably leads to restricted rotation around the C–NMe₂ bond and thus to the observed broadening.

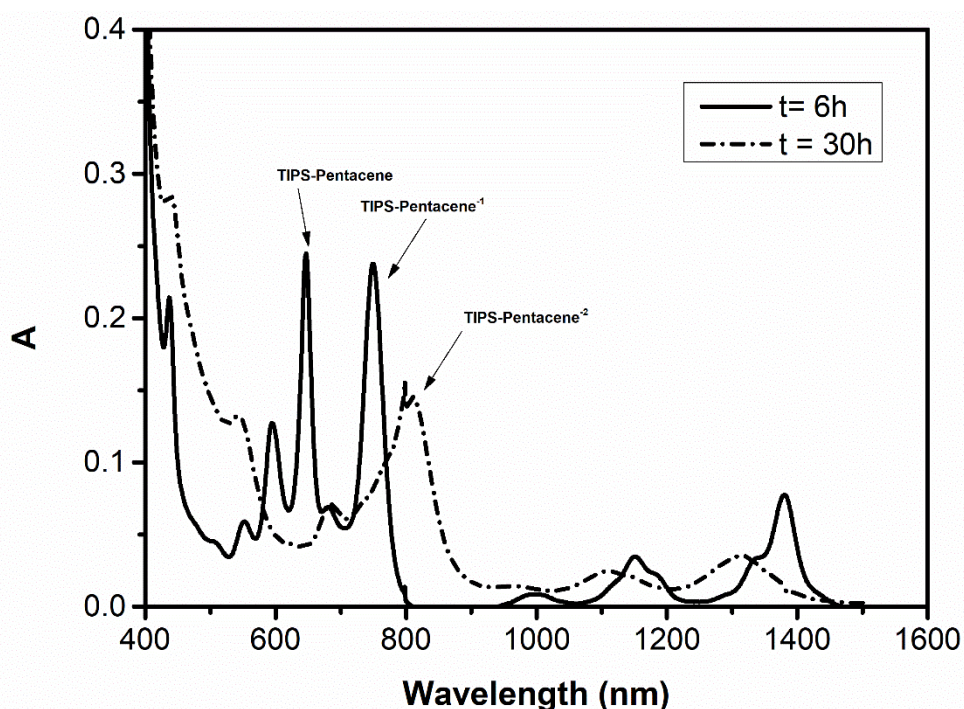## S5. Vis-NIR spectra from doping studies

Fig. S12. Absorption spectra in chlorobenzene containing initial concentrations of 1.5×10^{-4} M in **IV** (TIPS-pentacene) and 1.5×10^{-3} M in **4₂b** at various time (*t*) after mixing.

S6. Additional details and discussion of DFT results

Discussion of cation and neutral monomer geometry. Firstly we note that the DFT-optimized structure for **4⁺** reproduces the slight bending of the amino-substituted carbons away from the metal (fold angles β are 9.7 and 10.0° can be compared with the values in Table 1). The DFT-optimized structure of the neutral **4** monomer exhibits a much larger distortion of the arene ring from planarity. Although 19-electron sandwich compounds are in principle subject to Jahn-Teller effects, and we have seen distortions from axial symmetry in other DFT calculations of heavy-metal 19-electron monomers, the distortion for **4** is particularly large. Thus, while in the case of **1** (and **2**) the arene ring is planar, the arene in **4** is effectively η^4, with one of the amino-substituted carbon atoms and one of its adjacent unsubstituted carbons both at ca. 2.70 Å from the Ru. The structure could be regarded as an 18-electron RuCp*(η^4-diene)⁻ moiety linked to an uncoordinated CH•–CH=NMe₂⁺/CH=CH–NMe₂•⁺ moiety, or as a 17-electron neutral RuCp*(η^4-diene) moiety linked to an uncoordinated CH=CH–NMe₂

unit. The calculated spin densities are largest on the metal and on the uncoordinated CH carbon atom (Fig. S13) and, despite the differences in molecular geometry, are similar to those in **1**. The large spin density on the CH may contribute, along with steric effects, to kinetically favoring dimerization through the CH positions.
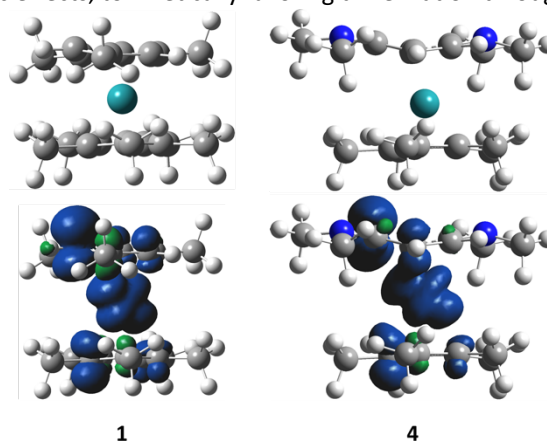

1   **4**

Fig. S13. Optimized geometries and (bottom) spin density distributions of **1** and **4** as determined at the M06/6–31G**/LANL2DZ level of theory.
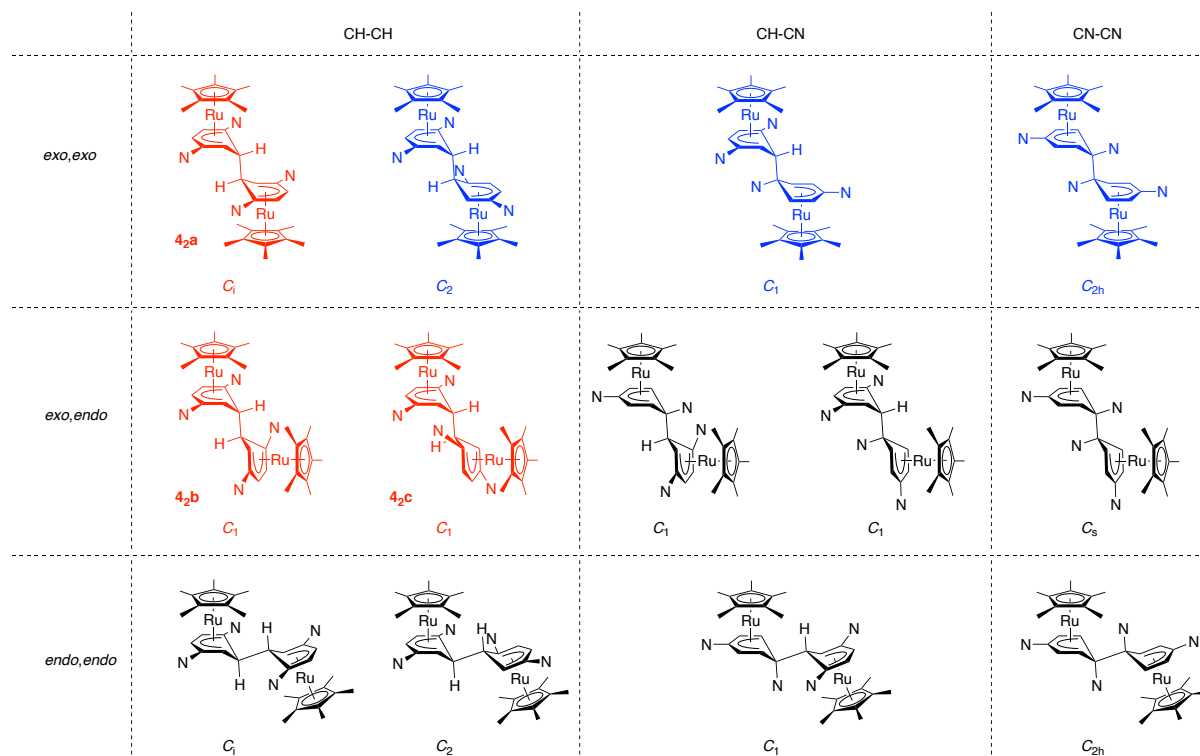

Fig. S14. Arene-arene linked isomers possible for **4$_2$**, along with the highest symmetry point groups that can be adopted in each case. Note that isomers with C_1 and C_2 symmetry will exist as pairs of enantiomers. Those shown in red have been isolated in this work; those shown in blue are also considered in the calculations (Tables 4 and S2). Note that NMe$_2$ is shortened to N here to avoid overly congested figures.

Table S2. DFT-Calculated Characteristics of Isomers of 4_2 in Dielectric Continuum Representing THF [a]

		Central C–C bond length / Å		relative stability / kJ mol⁻¹		$D_2 = D_2^{•+} + e^-$ / eV		$D_2 = 2D^•$ / kJ mol⁻¹		$D_2^{•+} = D^• + D^+$ / kJ mol⁻¹	
		D_2	$D_2^{•+}$	G	U	ΔG	ΔU	ΔG	ΔU	ΔG	ΔU
exo,exo-CHCH (**a**)	C_i	1.551	1.649	0	0	3.72	3.61	+95.3	+194.3	−42.9	+28.6
exo,exo-CHCH	C_2	1.550	1.641	+1.9	+6.9	3.64	3.71	+93.4	+187.4	−47.6	+22.2
exo,exo-CHCN	C_1	1.573	3.210	+43.3	+46.3	2.81	3.06	+52.0	+148.0	−9.3	+45.1
exo,exo-CNCN	C_{2h}	1.598	3.210	+114.2	+108.6	2.11	2.34	−18.9	+85.7	−12.4	+52.5
exo,endo-CHCH (**b**)	C_1	1.562	1.573	+24.7	+28.0	3.98	3.99	+70.6	+166.3	−103.4	−25.6
exo,endo-CHCH (**c**)	C_1	1.565	1.582	+40.2	+36.4	3.91	3.97	+55.1	+157.9	−112.2	−32.2

[a] ΔG and ΔU for $D^• = D^+$ are 2.18 and 2.00 eV, respectively.

Discussion of Dimer Frontier Molecular Orbitals. The orbitals for **4₂a** are qualitatively similar to those calculated for other *exo,exo* organometallic dimers including **1₂** and $[RhCp*Cp]_2$:[7] the HOMO and HOMO–1 can be regarded respectively as in-phase and out-phase combinations of the HOMOs of two RuCp*(η^5-pentadienyl) fragments, the HOMO being substantially destabilized relative to the HOMO–1 by out-of-phase interactions with the σ bonding orbital associated with the central C—C bond of the dimer. In this particular dimer, the HOMO is also destabilized through interactions with the N pπ orbitals of the NMe₂ substituents adjacent to the C—C bond, while both sets of amino groups contribute to the HOMO–1.

The orbitals for **4₂b** are different in that the HOMO and HOMO–1 are respectively localized on the *exo-* and *endo-* connected monomers, there is a smaller energetic separation between them than in **4₂a**, and the HOMO is lower in energy than in **4₂a** (consistent with the higher IE given in Table 3 and the less cathodic D₂⁺/D₂ redox potential in Table 1) The localization is partly a consequence of the inequivalence of the two monomer units, but also indicates a weaker electronic coupling between the two sites). The C—C σ-orbital only contributes to the HOMO, whereas the σ-orbital associated with the exo-C—H bond of the *endo*-connected monomer contributes to the HOMO–1, so that the HOMO–1 resembles the HOMO of a RuCp* cyclohexadienyl derivative.[7] Clearly, the local HOMO of each pentadienyl fragment can interact strongly with the σ-orbital associated with the bond that is *exo* relative to the metal, but not that of the *endo* bond, which prevents the local HOMOs of the two monomers being effectively coupled through the C—C bridge. These orbital observations are also consistent with the reactivity of different isomers of RhCp(η^4-Cp*H); EI mass spectrometry of *exo*-H and *endo*-H (i.e., *exo*-Me) isomers show base peaks corresponding to (M – H)⁺ and (M – Me)⁺ respectively.[8]

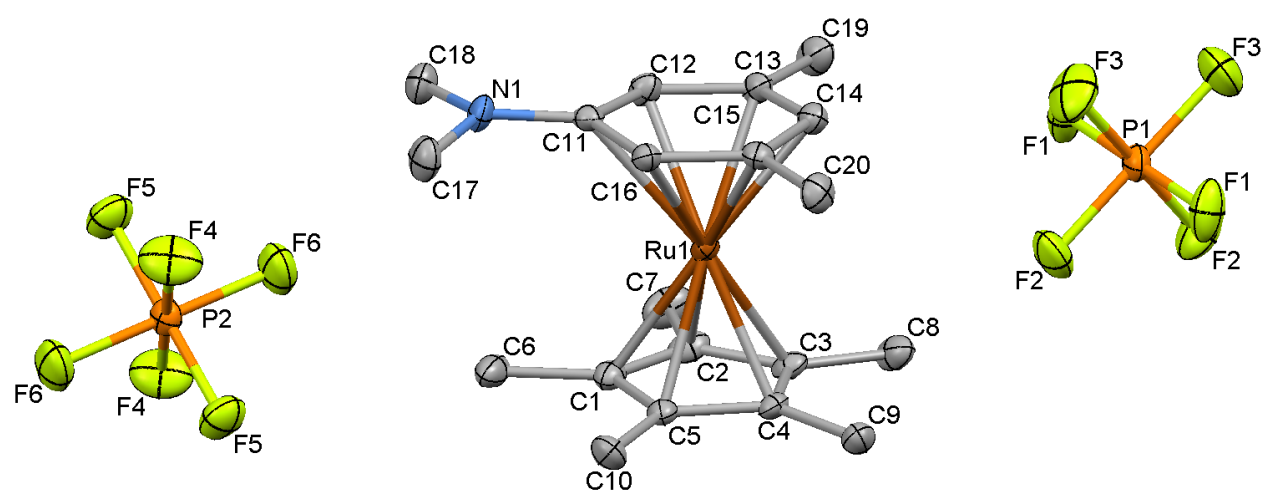## S7. Atomic numbering schemes for crystal structures

Fig. S15. Atomic labeling scheme for the crystal structure of **3**⁺[PF₆]⁻ (50% thermal ellipsoids, hydrogens excluded). Note that the asymmetric unit contains one cation and two half anions, the phosphorus atoms of which are located on either a crystallographic two-fold rotation axis (P1) or a crystallographic inversion center (P2).
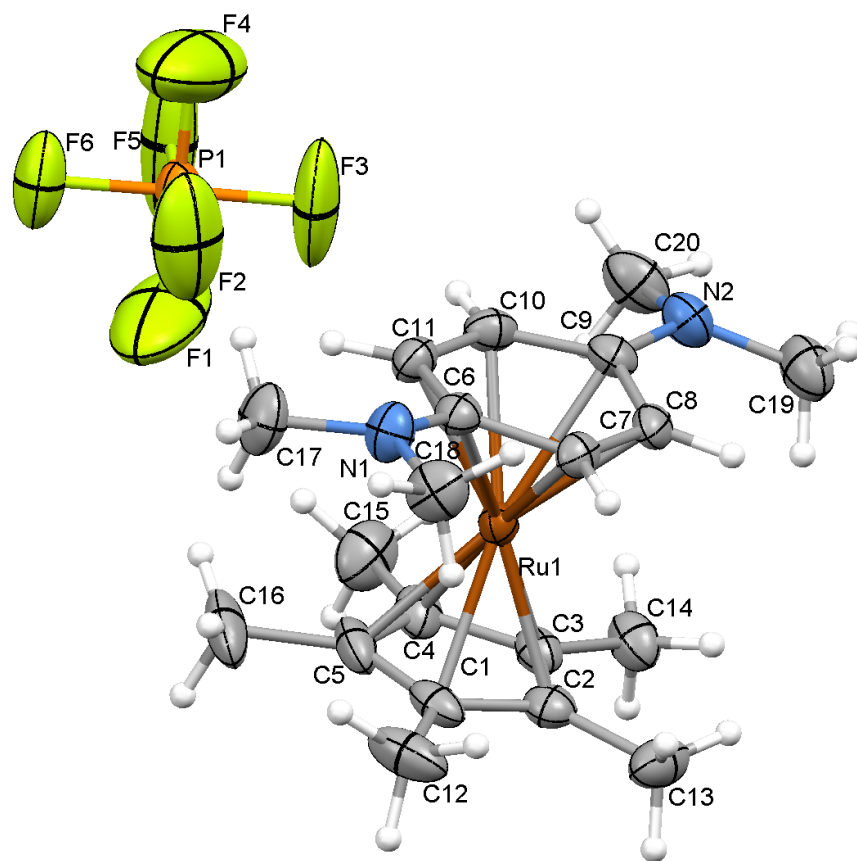
Fig. S16. Atomic labeling scheme for the crystal structure of **4**⁺[PF₆]⁻ (50% thermal ellipsoids). The asymmetric unit contains one cation and one anion.
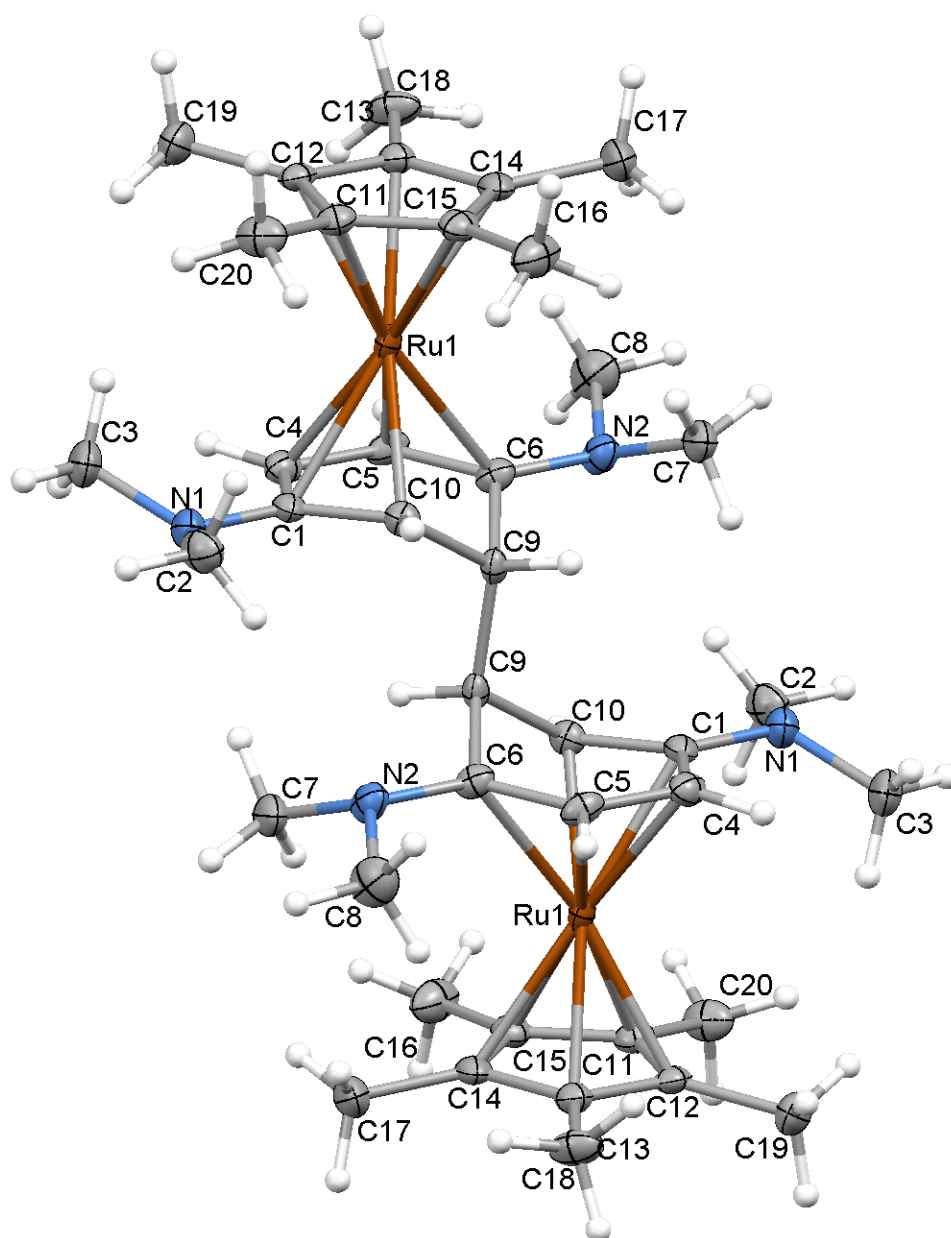
Fig. S17. Atomic labeling scheme for the crystal structure of **4₂a** (50% thermal ellipsoids). The asymmetric unit contains one half molecule, the molecule being located on a crystallographic inversion center.
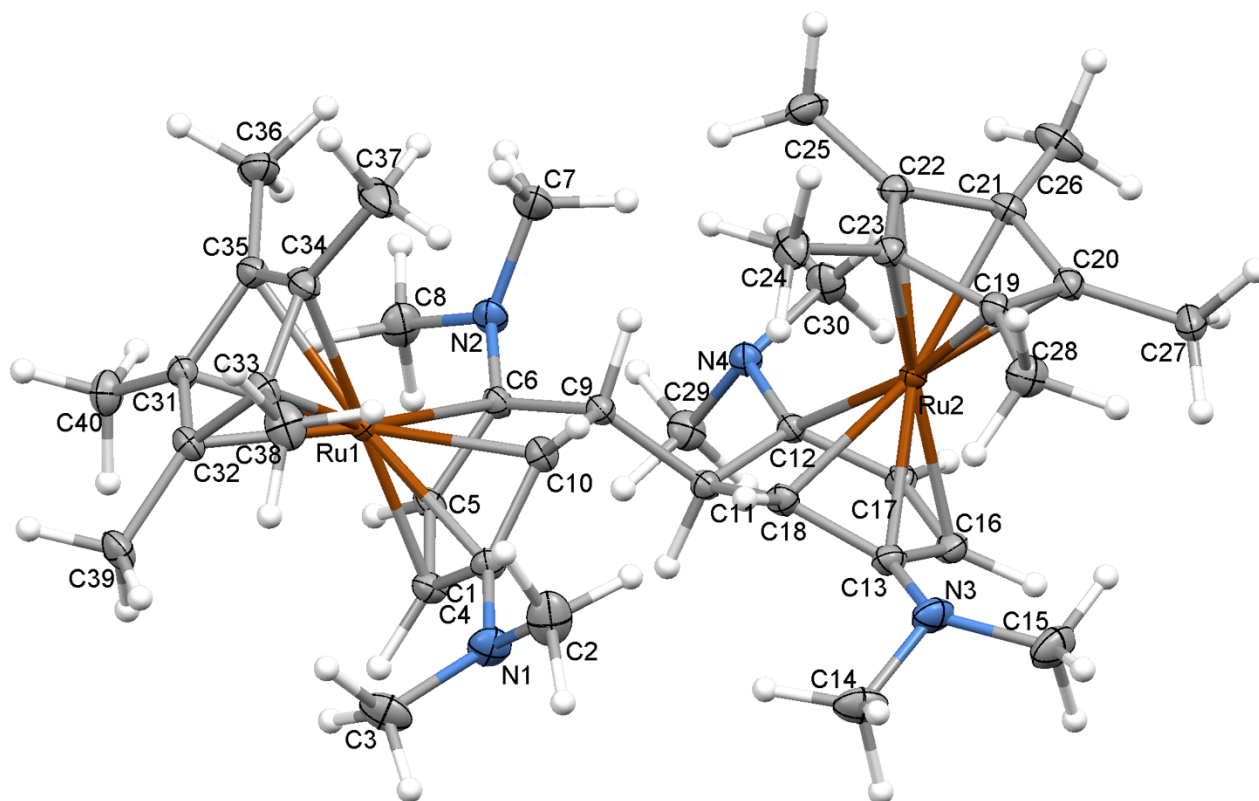
Fig. S18. Atomic labeling scheme for the crystal structure of **4₂b** (50% thermal ellipsoids). The asymmetric unit contains one molecule.

S8. References for ESI

1. S. K. Mohapatra, A. Romanov, T. V. Timofeeva, S. R. Marder and S. Barlow, *J. Organomet. Chem.*, 2014, **751**, 314.
2. A. I. Konovalov, E. O. Gorbacheva, F. M. Miloserdov and V. V. Grushin, *Chem. Commun.*, 2015, **51**, 13527-13530.
3. U. Koelle, M. H. Wang and G. Raabe, *Organometallics*, 1991, **10**, 2573.
4. S. D. Loren, B. K. Campion, R. H. Heyn, T. D. Tilley, B. E. Bursten and K. W. Luth, *J. Am. Chem. Soc.*, 1989, **111**, 4712.
5. O. V. Gusev, M. A. Ievlev, M. G. Peterleitner, S. M. Peregudova, L. I. Denisovich, P. V. Petrovskii and N. A. Ustynyuk, *J. Organomet. Chem.*, 1997, **534**, 57.
6. S. Guo, S. B. Kim, S. K. Mohapatra, Y. Qi, T. Sajoto, A. Kahn, S. R. Marder and S. Barlow, *Adv. Mater.*, 2012, **24**, 699.
7. S. K. Mohapatra, A. Fonari, C. Risko, K. Yesudas, K. Moudgil, J. H. Delcamp, T. V. Timofeeva, J.-L. Brédas, S. R. Marder and S. Barlow, *Chem. Eur. J.*, 2014, **20**, 15385.
8. K. Moseley, J. W. Kang and P. M. Maitlis, *J. Chem Soc. A*, 1970, 2875.